[20] Niwa H, Ogawa K, Shimosato D, Adachi K. A parallel circuit of LIF signalling pathways maintains pluripotency of mouse ES cells. Nature 2009; 460(7251):118–22.
[21] Alberti K, Davey RE, Onishi K, George S, Salchert K, Seib FP, et al. Functional immobilization of signaling proteins enables control of stem cell fate. Nat Methods 2008;5(7):645–50.
[22] Kim K, Doi A, Wen B, Ng K, Zhao R, Cahan P, et al. Epigenetic memory in induced pluripotent stem cells. Nature 2010;467(7313):285–90.
[23] Ying QL, Wray J, Nichols J, Batlle-Morera L, Doble B, Woodgett J, et al. The ground state of embryonic stem cell self-renewal. Nature 2008;453(7194):519–23.
[24] Jaenisch R, Young R. Stem cells, the molecular circuitry of pluripotency and nuclear reprogramming. Cell 2008;132(4):567–82.
[25] Hall J, Guo G, Wray J, Eyres I, Nichols J, Grotewold L, et al. Oct4 and LIF/Stat3 additively induce Kruppel factors to sustain embryonic stem cell self-renewal. Cell Stem Cell 2009;5(6):597–609.
[26] Hanna J, Cheng AW, Saha K, Kim J, Lengner CJ, Soldner F, et al. Human embryonic stem cells with biological and epigenetic characteristics similar to those of mouse ESCs. Proc Natl Acad Sci U S A 2010;107(20):9222–7.
[27] Buecker C, Chen HH, Polo JM, Daheron L, Bu L, Barakat TS, et al. A murine ESC-like state facilitates transgenesis and homologous recombination in human pluripotent stem cells. Cell Stem Cell 2010;6(6):535–46.
[28] Zhou H, Li W, Zhu S, Joo JY, Do JT, Xiong W, et al. Conversion of mouse epiblast stem cells to an earlier pluripotency state by small molecules. J Biol Chem 2010;285:29676–80.

UICC
global cancer control

IJC
International Journal of Cancer

Antitumor effect of sunitinib against skeletal metastatic renal cell carcinoma through inhibition of osteoclast function

Shinya Maita[1], Takeshi Yuasa[1,2,3], Norihiko Tsuchiya[1], Yoko Mitobe[1], Shintaro Narita[1], Yohei Horikawa[1], Kiyohiko Hatake[2], Iwao Fukui[3], Shinya Kimura[4], Taira Maekawa[5] and Tomonori Habuchi[1]

[1] Department of Urology, Akita University School of Medicine, Akita, Japan
[2] Department of Medical Oncology, Cancer Institute Hospital, Japanese Foundation for Cancer Research, Ariake, Tokyo, Japan
[3] Department of Urology, Cancer Institute Hospital, Japanese Foundation for Cancer Research, Ariake, Tokyo, Japan
[4] Department of Hematology, Saga University School of Medicine, Saga, Japan
[5] Department of Transfusion Medicine and Cell Therapy, Kyoto University Hospital, Kyoto, Japan

We investigated the inhibitory effect of sunitinib, a newly approved multitargeted tyrosine kinase inhibitor, against the progression of renal cell cancer (RCC) bone metastases *in vivo*. *In vitro* cell proliferation was determined using the MTS assay. To investigate the inhibitory effects of sunitinib *in vivo*, we established luciferase-labeled ACHN^{Luc} cells derived from papillary RCC. Mice in which ACHN^{Luc} cells had been transplanted into the left ventricle to establish bone metastases were treated orally with 40 mg/kg/day sunitinib or vehicle control for 3 weeks. Growth of the cancer cells was monitored using an *in vivo* imaging system. In addition, 16 patients with metastatic RCC were treated with sunitinib, and serum and urine levels of amino-terminal telopeptide (NTx) were measured as markers of bone resorption. Sunitinib did not inhibit the growth of RCC cells *in vitro* at clinically or experimentally achievable serum levels (100 nM–1 μM). To investigate the inhibitory effect of sunitinib *in vivo*, we established luciferase-labeled human RCC cells (ACHN^{Luc}). Sunitinib prevented the growth of ACHN^{Luc} RCC cells in the bone metastatic mouse model. The number of osteoclasts in sunitinib-treated mice was significantly less than that in control mice. Serum and urine levels of NTx in patients with metastatic RCC declined significantly during the first 4 weeks of sunitinib treatment ($p = 0.027$). Sunitinib is a potent anticancer agent for RCC bone metastases, at least for papillary RCC.

Bone is a common site of metastasis, with the frequency of solitary or multiple metastases to bone ranging from 24 to 51% in patients with metastatic renal cell cancer (RCC).[1–3] Although bone metastasis is not an independent prognostic factor associated with poor survival, the prognosis of patients with bone metastasis is not favorable when they are treated with cytokines, with an average life expectancy of 8–16 months.[2–4] Moreover, bone metastases are associated with poor performance status due to intractable pain and pathological fractures.[5] Because treatment options for RCC patients with bone metastasis are limited, appropriate treatment strategies are desired.

Sunitinib is a newly approved, multitarget, small-molecule tyrosine kinase inhibitor for the treatment of metastatic RCC. It inhibits various receptor tyrosine kinases, including vascular endothelial growth factor (VEGF) receptors 1, 2 and 3; stem cell factor receptor (KIT) and PDGF receptors α and β.[6–8] Moreover, sunitinib has been known to inhibit the phosphorylation of colony-stimulating factor (CSF)-1R, resulting in the prevention of osteoclast function and CSF-1R-dependent osteolysis in an experimental breast cancer bone metastasis model.[9,10] These findings led us to propose the hypothesis that sunitinib may inhibit tumor growth and osteolysis in bone metastatic lesions in RCC patients.

Although establishing a treatment strategy for bone metastases from RCC is important for urologists, the assessment of inhibitory effects on the growth of bone metastases is often difficult in clinical practice. In this study, we show that sunitinib has anticancer as well as inhibitory activities against osteolysis in an experimental mouse model of bone metastasis of RCC cells.

Key words: renal cell carcinoma, bone metastases, sunitinib, *in vivo* imaging system
Grant sponsors: Takeda Science Foundation, The Kobayashi Institute for Innovative Cancer Chemotherapy, The Shimadzu Science Foundation, The Sagawa Foundation for Promotion of Cancer Research, Grants-in-Aid for Scientific Research from the Ministry of Education, Culture, Sports, Science and Technology, Japan and the GCOE program of the Ministry of Education, Culture, Sports, Science and Technology, Japan
DOI: 10.1002/ijc.26034
History: Received 15 Jun 2010; Revised 4 Jan 2011; Accepted 26 Jan 2011; Online 8 Mar 2011
Correspondence to: Takeshi Yuasa, Department of Medical Oncology and Genitourinary Oncology, Cancer Institute Hospital, Japanese Foundation for Cancer Research, Ariake, Tokyo 135-8550, Japan, E-mail: takeshi.yuasa@jfcr.or.jp

Material and Methods

Animals, cell lines and reagents

Approval for these studies was obtained from the institutional review board at Akita University School of Medicine. Specific pathogen-free BALB/c *nu/nu* mice (CLEA, Kyoto, Japan) aged 7 weeks were used. The human RCC lines ACHN, CCFRC-1, CCFRC-2 and NC65 were obtained from the American Type Culture Collection (ATCC, Rockville, MD) and sunitinib was obtained from Pfizer (New York, NY).

Patients

A total of 16 native Japanese patients with metastatic RCC, who were treated at the Department of Urology at Akita University School of Medicine between 2008 and 2009, were enrolled, and the serum and urine levels of amino-terminal telopeptide (Serum NTx, normal range: 9.5–17.7 nmol/l) were measured as markers of bone resorption. The patients' characteristics are shown in Table 1. The median dose was 37.5 (25–50) mg/day and the median number of treatment cycles was 4.6 (1–21). Written informed consent was provided according to the Declaration of Helsinki. The study protocol was approved by the Ethics Committee of Akita University Graduate School of Medicine. The response was assessed by computed tomography (CT) after at least every two cycles of treatment, according to the Response Evaluation Criteria in Solid Tumors (RECIST ver. 1.0).[11]

Growth inhibitory effects of sunitinib in vitro

Cell proliferation was determined by the MTS assay using CellTiter96 (Promega Corporation, Madison) as described previously.[12]

Generation of a stable luciferase-expressing cancer cell line

Among the RCC cell lines we tested (ACHN, CCFRC-1, CCFRC-2 and NC65), ACHN was the only line that was transplanted into the left ventricle and formed bone metastases successfully. Therefore, we used $ACHN^{Luc}$ in the *in vivo* experiment. ACHN cells were stably transfected with the pGL3 control vector (Promega Corporation, Madison) and with pSV2Neo (ATCC), as described previously.[12] In brief, the cells were treated with 10 μg pGL3 control vector and 1 μg pSV2Neo vector using Lipofectamine 2000 (Invitrogen, Carlsbad, CA) in Opti-MEM (Invitrogen) and selected using geneticin (400 μg/ml). Stable clones expressing luciferase were isolated and the clone with the highest level of luciferase expression (as determined by bioluminescence) was selected using luciferin (Xenogen, Alameda, CA) and an *in vivo* imaging system (IVIS; Xenogen).

In vivo effects of sunitinib

To produce bone metastasis models, RCC cell suspensions (3×10^6/100 μl phosphate-buffered saline) were injected into the left ventricle of mice under inhalation anesthesia with isoflurane (Abbott Japan, Tokyo, Japan). From 21 days after implantation, 14 mice with bone metastases were selected and divided into two matched groups on the basis of bioluminescence quantified by IVIS. On the same day, we started daily oral administration of 40 mg/kg (body weight) sunitinib or the solution used to dissolve sunitinib as vehicle control. According to the human 4 weeks on/2 weeks off schedule, mice were treated with sunitinib for 4 weeks before being sacrificed. Mice were observed by IVIS once per week.

Table 1. Patients characteristics

Factors			
Age (years old)	Median	60.5	Range: 37–80
Sex (*n*)	Male	13	(81%)
	Female	3	(19%)
Metastatic sites	Lung	12	(75%)
	Liver	4	(25%)
	Bone	5	(31%)
	Brain	3	(19%)
	Lymph node	3	(19%)
Follow-up period (month)	Median	4.5	Range: 1–37
Performance status	0 or 1	15	(94%)
	>1	1	(6%)
Diagnosis to initial treatment	>1 year	5	(31%)
	<1 year	11	(69%)
Blood hemoglobin	Normal range	7	(44%)
	ULN>	9	(56%)
Serum calcium	<10 mg/dl	15	(94%)
	≥10 mg/dl	1	(6%)
Serum LDH	<1.5 × ULN	16	(100%)
	≥1.5 × ULN	0	(0%)
MSKCC risk classification	Favorable	6	(38%)
	Intermediate	9	(56%)
	Poor	1	(6%)

ULN: upper limit of normal range.

Measurement of bone metastatic lesions by in vivo imaging

An aqueous solution of luciferin (150 mg/kg) was injected intraperitoneally 10 min before imaging. The animals were anesthetized with isoflurane and placed in the light-tight chamber of a CCD camera system (Xenogen) and photons emitted from the luciferase-expressing cells within the animal were quantified for 5 min using the software program Living Image (Xenogen) as an overlay on Igor (Wavemetrics, Seattle, WA). Using this *in vivo* imaging system, we evaluated the efficacy of sunitinib by measuring the photon counts of the metastatic lesions in the mandible and both hip joints in a blinded manner as described previously.[13]

Measurement of serum VEGF and M-CSF in the mouse bone metastasis model in vivo

The serum concentrations of VEGF and M-CSF in mice were determined using Quantikine ELISA (R&D Systems, Minneapolis, MN) according to the manufacturer's protocol. To investigate the serum concentrations of VEGF and M-CSF, sera from each of seven treated and seven untreated mice were collected and analyzed 4 weeks after $ACHN^{Luc}$ inoculation.

Histological analysis

After imaging studies, the femora of the mice were removed, frozen immediately and stored at −80°C. To detect osteoclasts, 4-μm-thick sections were stained with tartrate-resistant acid phosphatase (TRAP) using the TRAP and ALP double-stain kit (Takara Bio, Otsu, Japan), as described previously.[14] Three sections were examined in each femur. The number of TRAP-positive osteoclasts was counted per ten high-power microscope fields by two blinded examiners, as described previously.[14]

Statistical analysis

The influence of sunitinib on the growth of bone metastases was analyzed by Student's *t* test. All statistical analyses were performed using the Statistical Package for the Social Sciences (SPSS version 13.0; SPSS, Chicago, IL), and two-sided *p* values <0.05 were considered statistically significant.

Results

Effect of sunitinib on RCC growth in a mouse bone metastasis model in vivo

Injection of cancer cells via the left ventricle is an established method of inducing bone metastases, as reported previously.[12,13] In the present study, all mice that were successfully implanted with $ACHN^{Luc}$ cancer cells developed bone metastases 3 weeks after injection. Of these mice, we excluded those that showed brilliant bioluminescence in the lungs. The remaining 14 mice were then divided into two matched groups according to bioluminescence quantified by IVIS, and we administered either sunitinib or vehicle control for 4 weeks and monitored the growth of bone metastases in the lesions in the maxilla and bilateral hip joints, as described previously[12,13] (Fig. 1*b*). Metastatic bone lesions in the control group progressed during the 3 weeks. On the other hand, photon emission was significantly suppressed in the sunitinib treatment group ($p < 0.001$) (Figs. 1*a* and 1*c*). The mean body weights of the mice did not differ significantly between the two groups.

Serum VEGF and M-CSF in a mouse bone metastasis model in vivo

To examine the indirect antitumor effect of sunitinib, we measured the concentrations of VEGF and M-CSF. However, no significant difference was present in the serum concentrations of these growth factors between the two groups (Fig. 1*d*).

Effect of sunitinib on osteoclasts in a mouse bone metastasis model

Next, we investigated the efficacy of sunitinib against osteoclasts in the tumor-bearing mice. Femoral bone sections were stained with TRAP to enable counting of the number of osteoclasts, as described previously.[13] The mean number of TRAP-positive osteoclasts in mice treated with sunitinib was significantly lower than that in mice treated with vehicle control (23.1 ± 4.7 *vs.* 33.2 ± 7.9 osteoclasts/100 high-power fields, respectively; $p = 0.013$).

Sunitinib did not inhibit cell proliferation in vitro at a clinically achievable serum concentration

To assess the direct antitumor effect of sunitinib, four RCC cell lines (ACHN, CCFRC-1, CCFRC-2 and NC65) were cultured in the presence of various concentrations of sunitinib (0.1 nM–10 μM). Sunitinib inhibited the proliferation of these cell lines in a concentration-dependent manner (Fig. 2). However, sunitinib was not effective *in vitro* at the clinically achievable serum concentration (~80 nM), as demonstrated previously.[8] On the other hand, the serum concentration of sunitinib was reported to be ~100 nM on administration to mice at 40 mg/kg/day.[14] The IC50s of sunitinib for these cell lines were estimated to be >1 μM. These results suggest the involvement of an indirect growth inhibitory mechanism of sunitinib, at least partially, for bone metastatic lesions in mice.

Effect of sunitinib on serum and urine levels of NTx in patients with metastatic RCC

The characteristics and demographic data of the patients are shown in Table 1. As shown in Figure 3, both serum and urine levels of NTx significantly declined during the first 4 weeks of treatment with sunitinib ($p = 0.027$). During the holiday period when the administration was discontinued following 4 weeks of administration of sunitinib, the serum and urine levels of NTx showed gradual recovery (Fig. 3). Of these 16 patients, five had bone metastatic lesions, but we could not evaluate the efficacy of sunitinib quantitatively. Regarding the extraosseous sites, nine of 14 patients demonstrated a partial response (PR) or stable disease (SD) whereas the remaining five demonstrated progressive disease (PD). The reduction rate of the serum NTx level from the baseline in patients with favorable efficacy (PR/SD; 30.8%) was higher than that in patients with poor efficacy (PD; 22%), although the difference was not significant ($p = 0.6404$).

Discussion

In patients with metastatic RCC, bone is the major metastatic organ, second only to the lung.[1–3] Bone metastases were shown to be associated with severe bone pain, pathological fractures, spinal cord compression and a short survival

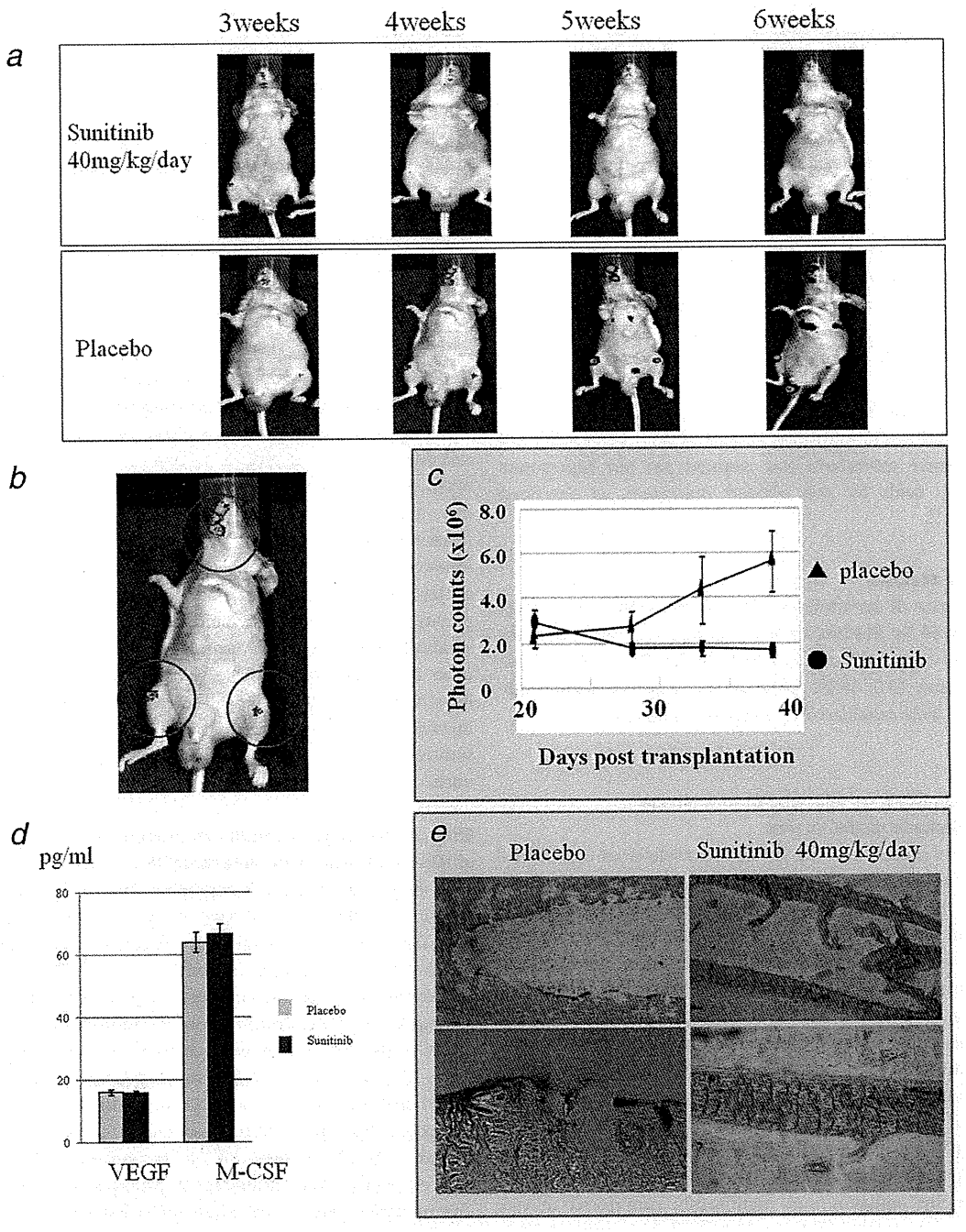

Cancer Therapy

Figure 1. Growth inhibitory effect of orally administered sunitinib in an RCC bone metastatic mouse model. We established an RCC bone metastatic mouse model using the cell line ACHN^{Luc}. Images were obtained using an *in vivo* imaging system 3–6 weeks after cell transplantation by intracardiac injection (*a*). To evaluate the growth inhibitory effect of orally administered sunitinib, we selected metastatic lesions from the maxilla and bilateral hip joints as examples of bone metastasis (*b*). Average real-time growth curves of ACHN^{Luc} cells of bone metastatic lesions in sunitinib- and control vehicle-treated groups demonstrated that sunitinib significantly prevented the growth of metastatic bone lesions ($p < 0.001$; *c*). Serum levels of VEGF and M-CSF did not differ significantly between sunitinib-treated and control mice (*d*). The mean number of TRAP-positive osteoclasts in mice treated with sunitinib was significantly lower than that in mice treated with vehicle control ($p = 0.013$; *e*).

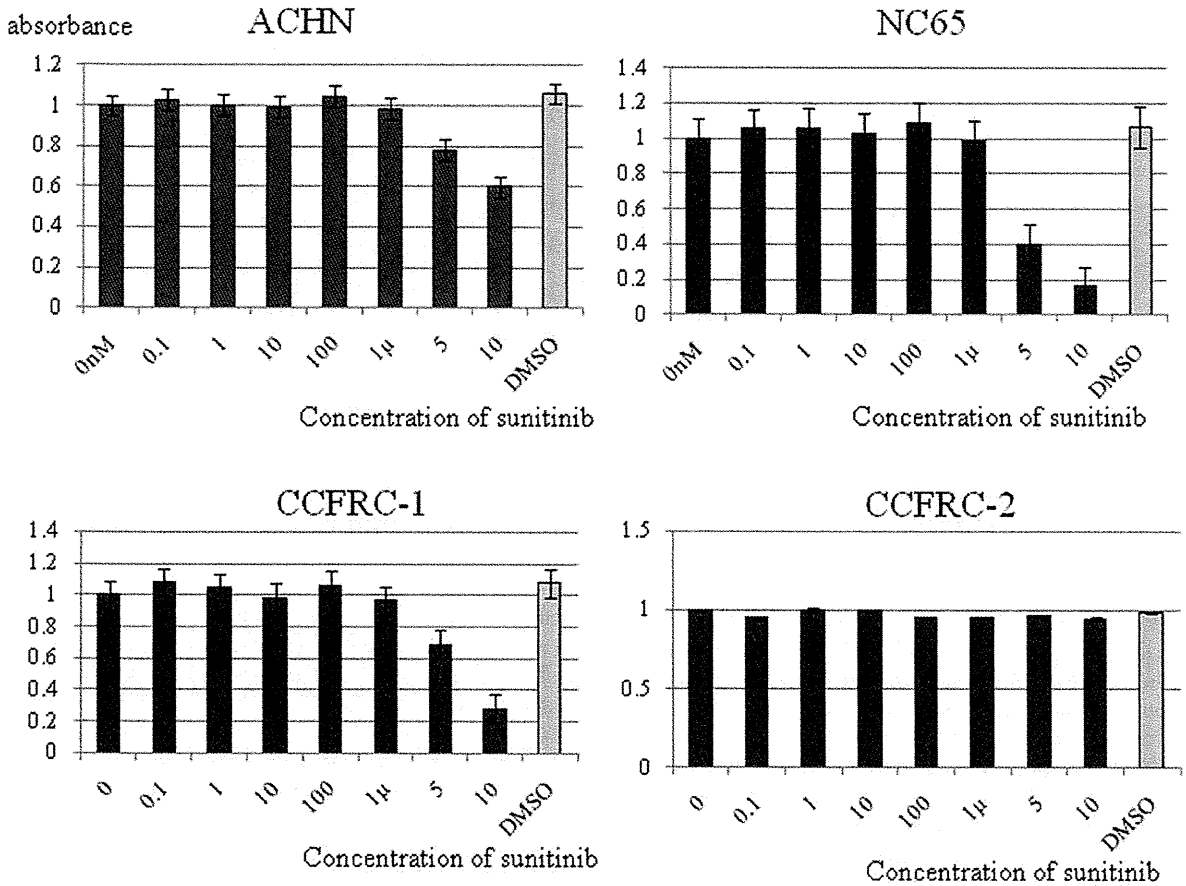

Figure 2. Sunitinib does not inhibit the growth of RCC at a clinically achievable concentration *in vitro*. Cells of the RCC lines ACHN, NC65, CCFRC-1 and CCFRC-2 were plated at 3,000 cells/well in 96-well plates, incubated for 24 hr, and then treated with various concentrations (0–100 mM) of sunitinib. After 72 hr of incubation, relative cell growth was measured in an MTS assay. Data are Mean ± SD. Sunitinib did not inhibit the growth of any of the four RCC cell lines at the clinically achievable concentration (~80 nM) *in vitro*.

period.[4,11] Several studies have demonstrated that bone metastasis is one of the risk factors for poor prognosis in the cytokine era, although it was not identified as an independent prognostic factor.[1–4] Négrier *et al.* investigated the prognostic factors of 782 metastatic RCC patients treated with cytokines and found that 32% (248/776) had bone metastases, and that these patients had a significantly worse prognosis than those without bone metastases ($p = 0.008$).[2] Recently, Naito *et al.* retrospectively analyzed the prognosis of 1,463 Japanese metastatic RCC patients in the cytokine era and demonstrated that 24.6% (320/1,302) had bone metastases, and that these patients also had a significantly worse prognosis than those without bone metastases ($p = 0.003$).[3] Accumulated evidence suggests that systemic immunotherapy is not effective in the management of bone metastasis of RCC.

The efficacy of sunitinib against RCC bone metastasis, however, remains to be established and is difficult to evaluate in clinical practice. Thus, we sought to investigate the efficacy of sunitinib against bone metastatic RCC in the preclinical setting. The dose of sunitinib used in this study (40 mg/kg/day) was intended to provide a serum level of sunitinib similar to that attained in the clinical setting.[8,15] Pharmacokinetic and pharmacodynamic analyses showed that the clinical dose of 50 mg/day led to plasma concentrations ranging from 50 to 100 ng/ml in humans.[8] This dose is equivalent to the plasma concentration in mice administered sunitinib at 40 mg/kg/day.[15] Data from VEGF-induced vascular permeability assays also support 50–100 ng/ml as the range, including the minimum plasma concentrations required to inhibit VEGFR and PDGFR *in vivo*.[8] Therefore, our results obtained in the RCC bone metastatic model used in this study might be reflective of those obtained in the clinical setting.

Similar to several other *in vitro* analyses, our results showed that sunitinib at concentrations of 50–100 ng/ml did not inhibit the proliferation of RCC cells *in vitro*.[10,16] Therefore, we sought an indirect mechanism for this *in vivo* growth inhibition of RCC bone metastases. Bone is an abundant repository for immobilized growth factors, including

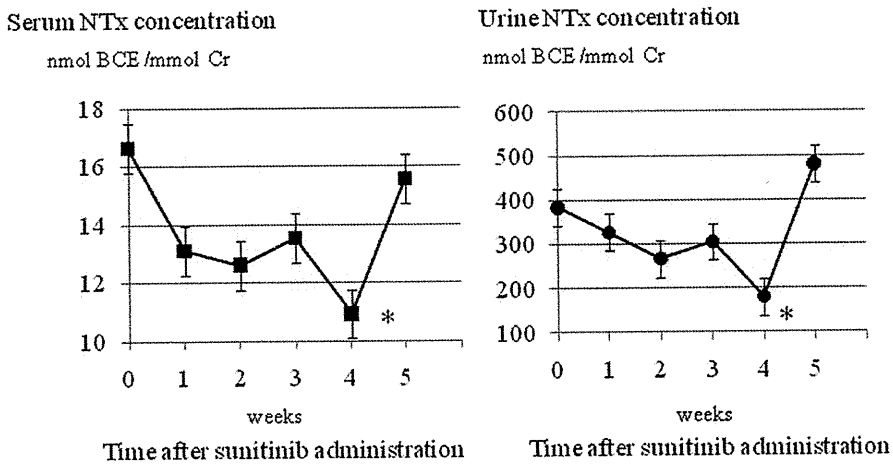

Figure 3. Alteration of bone resorption markers in sunitinib-treated patients with metastatic RCC. Serum and urine levels of NTx 28 days after oral administration of sunitinib were significantly lower than initial levels (*$p < 0.01$). Characteristics of the 16 sunitinib-treated patients are shown in Table 1.

transforming growth factor beta, fibroblast growth factor, insulin-like growth factors I and II, PDGF and bone morphogenetic proteins.[17] When osteoclasts absorb bone by secreting protons and proteases, these growth factors are released and they provide fertile ground for the growth of cancer cells. Therefore, osteoclasts are a suitable therapeutic target in the treatment of bone metastases. In this study, there were significantly fewer TRAP-positive osteoclasts in the mice treated with sunitinib than in those treated with vehicle control (Fig. 1*e*). This observation is consistent with previous reports.[10,18] Zwolak *et al.* reported that treatment with sunitinib decreased the percentage of active osteoclasts to 45.6% ± 5.8% compared with the percentage in untreated tumor-bearing mice (79.4% ± 8.6%), suggesting that sunitinib treatment (40 mg/kg/day) may inhibit osteoclast maturation.[18] Murray *et al.* reported that sunitinib inhibited osteoclast development and function mediated by M-CSF, which is one of the differentiating factors for osteoclasts and is a target tyrosine kinase of sunitinib, both *in vitro* and *in vivo*.[10] Our clinical observation of decreases in serum and urine NTx is also in line with these reports (Fig. 3).

NTx is a degradation product of Type I collagen and is often used as a marker of bone resorption both in serum and urine. Some clinical studies have suggested that levels of NTx correlate with the presence and extent of bone metastases, prognosis and response to treatment.[19,20] Although our data did not show an association between the reduction rate of NTx and the efficacy of sunitinib, further investigation is necessary to clarify this association, especially in bone metastatic lesions.

During the completion of this manuscript, we found that ACHN originated from papillary renal cancer in a 22-year-old patient (Reference [21] and by personal communication from Dr. Ernest Borden). Recent studies have suggested the possible clinical efficacy of sunitinib for patients with clear and non-clear cell cancer.[22,23] However, there are no prospective Phase 2 or Phase 3 studies clarifying this question. We therefore have to wait for the results of a large prospective study on the use of sunitinib for non-clear cell cancer. Since bone is the second most common site of metastases for RCC, we reported an indirect mechanism that may partly help to elucidate the reasons for the clinical efficacy of sunitinib.

Mesenchymal-epithelial transition factor (MET) and fumarate hydratase (FH) are considered to be the genes responsible for Type 1 and Type 2 papillary RCC, respectively.[24,25] MET, which is a proto-oncogene, encodes a tyrosine kinase membrane receptor, and activation of MET can indirectly promote angiogenesis and tumor growth through overexpression of VEGF.[26,27] FH is an enzyme in the mitochondrial tricarboxylic acid (TCA) cycle. Loss of FH leads to a state of pseudohypoxia through overexpression of hypoxia-inducible factor (HIF), resulting in an increase in downstream targets, including VEGF.[26,28] Therefore, activation of MET and loss of FH, which are considered to be responsible for Type 1 and Type 2 papillary RCC, lead to angiogenesis. Clinically, Ljungberg *et al.* demonstrated that the mRNA levels of VEGF, VEGF-receptor Type 1 and VEGF-receptor Type 2 above the median were related to adverse survival in papillary RCC.[29] Therefore, it is relevant to measure VEGF in a clear or non-clear cell RCC model.

To elucidate whether sunitinib has any other indirect effects, we measured the concentrations of VEGF and M-CSF. However, we found no significant difference between the two groups in the serum concentrations of these growth factors. This observation is consistent with previous findings. Ebos *et al.* reported a significant increase in the serum VEGF level on administration of 60–120 mg/kg sunitinib.[30] While it has been shown that sunitinib is a multikinase inhibitor that

inhibits Class III and Class V RTKs, including PDGF receptors, VEGF receptors, KIT and FLT3, with low nanomolar potency,[30] other growth factor-mediated signals might be inhibited by sunitinib. Further investigation is necessary to clarify the precise mechanism of action of sunitinib and its clinical efficacy against bone metastases.

Conclusion

In conclusion, we demonstrated that oral administration of a clinically achievable dose of sunitinib prevented the growth of RCC bone metastases *in vivo*. Because RCC cell lines are resistant to clinically and preclinically achievable plasma concentrations *in vitro*, prevention of osteoclast activity and/or maturation is one of the mechanisms of growth inhibition in metastatic bone lesions. Our study supports the use of sunitinib as an initial treatment for RCC patients with bone metastasis.

Acknowledgements

The authors thank Ms. Yuka Izumida and Ms. Tomomi Kawamura for their technical assistance.

References

1. Motzer RJ, Michaelson MD, Redman BG, Hudes GR, Wilding G, Figlin RA, Ginsberg MS, Kim ST, Baum CM, DePrimo SE, Li JZ, Bello CL, et al. Activity of SU11248, a multitargeted inhibitor of vascular endothelial growth factor receptor and platelet-derived growth factor receptor, in patients with metastatic renal cell carcinoma. *J Clin Oncol* 2006;24:16–24.
2. Négrier S, Escudier B, Gomez F, Douillard JY, Ravaud A, Chevreau C, Buclon M, Pérol D, Lasset C. Prognostic factors of survival and rapid progression in 782 patients with metastatic renal carcinomas treated by cytokines: a report from the Groupe Français d'Immunothérapie. *Ann Oncol* 2002;13:1460–68.
3. Naito S, Yamamoto N, Takayama T, Muramoto M, Shinohara N, Nishiyama K, Takahashi A, Maruyama R, Saika T, Hoshi S, Nagao K, Yamamoto S, et al. Prognosis of Japanese metastatic renal cell carcinoma patients in the cytokine era: a cooperative group report of 1463 patients. *Eur Urol* 2009; 3.
4. Toyoda Y, Shinohara N, Harabayashi T, Abe T, Akino T, Sazawa A, Nonomura K. Survival and prognostic classification of patients with metastatic renal cell carcinoma of bone. *Eur Urol* 2007;52: 163–8.
5. Kuczyk MA, Anastasiadis AG, Zimmermann R, Merseburger AS, Corvin S, Stenzl A. Current aspects of the surgical management of organ-confined, metastatic, and recurrent renal cell cancer. *BJU Int* 2005;96:721–7; quiz i–ii.
6. Oudard S, George D, Medioni J, Motzer R. Treatment options in renal cell carcinoma: past, present and future. *Ann Oncol* 2007; 18 (Suppl 10):x25–x31.
7. Hutson TE, Figlin RA, Kuhn JG, Motzer RJ. Targeted therapies for metastatic renal cell carcinoma: an overview of toxicity and dosing strategies. *Oncologist* 2008;13: 1084–96.
8. Faivre S, Delbaldo C, Vera K, Robert C, Lozahic S, Lassau N, Bello C, Deprimo S, Brega N, Massimini G, Armand JP, Scigalla P, et al. Safety, pharmacokinetic, and antitumor activity of SU11248, a novel oral multitarget tyrosine kinase inhibitor, in patients with cancer. *J Clin Oncol* 2006;24: 25–35.
9. Motzer RJ, Hoosen S, Bello CL, Christensen JG. Sunitinib malate for the treatment of solid tumours: a review of current clinical data. *Exp Opin Invest Drugs* 2006;15:553–61.
10. Murray LJ, Abrams TJ, Long KR, Ngai TJ, Olson LM, Hong W, Keast PK, Brassard JA, O'Farrell AM, Cherrington JM, Pryer NK. SU11248 inhibits tumor growth and CSF-1R-dependent osteolysis in an experimental breast cancer bone metastasis model. *Clin Exp Metastasis* 2003;20:757–66.
11. Therasse P, Arbuck SG, Eisenhauer EA, Wanders J, Kaplan RS, Rubinstein L, Verweij J, Van Glabbeke M, van Oosterom AT, Christian MC, Gwyther SG. New guidelines to evaluate the response to treatment in solid tumors. European Organization for Research and Treatment of Cancer, National Cancer Institute of the United States, National Cancer Institute of Canada. *J Natl Cancer Inst* 2000;92:205–16.
12. Yuasa T, Nogawa M, Kimura S, Yokota A, Sato K, Segawa H, Kuroda J, Maekawa T. A third-generation bisphosphonate, minodronic acid (YM529), augments the interferon alpha/beta-mediated inhibition of renal cell cancer cell growth both in vitro and in vivo. *Clin Cancer Res* 2005;11: 853–9.
13. Nogawa M, Yuasa T, Kimura S, Kuroda J, Sato K, Segawa H, Yokota A, Maekawa T. Monitoring luciferase-labeled cancer cell growth and metastasis in different in vivo models. *Cancer Lett* 2005;217:243–53.
14. Henriksen K, Tanko LB, Qvist P, Delmas PD, Christiansen C, Karsdal MA. Assessment of osteoclast number and function: application in the development of new and improved treatment modalities for bone diseases. *Osteoporos Int* 2007;18: 681–5.
15. Mendel DB, Laird AD, Xin X, Louie SG, Christensen JG, Li G, Schreck RE, Abrams TJ, Ngai TJ, Lee LB, Murray LJ, Carver J, et al. In vivo antitumor activity of SU11248, a novel tyrosine kinase inhibitor targeting vascular endothelial growth factor and platelet-derived growth factor receptors: determination of a pharmacokinetic/pharmacodynamic relationship. *Clin Cancer Res* 2003;9:327–37.
16. Sonpavde G, Jian W, Liu H, Wu MF, Shen SS, Lerner SP. Sunitinib malate is active against human urothelial carcinoma and enhances the activity of cisplatin in a preclinical model. *Urol Oncol* 2009;27: 391–9.
17. Yuasa T, Kimura S, Ashihara E, Habuchi T, Maekawa T. Zoledronic acid—a multiplicity of anti-cancer action. *Curr Med Chem* 2007;14:2126–35.
18. Zwolak P, Jasinski P, Terai K, Gallus NJ, Ericson ME, Clohisy DR, Dudek AZ. Addition of receptor tyrosine kinase inhibitor to radiation increases tumour control in an orthotopic murine model of breast cancer metastasis in bone. *Eur J Cancer* 2008;44:2506–17.
19. Brown JE, Cook RJ, Major P, Lipton A, Saad F, Smith M, Lee KA, Zheng M, Hei YJ, Coleman RE. Bone turnover markers as predictors of skeletal complications in prostate cancer, lung cancer, and other solid tumors. *J Natl Cancer Inst* 2005;97: 59–69.
20. Coleman RE, Major P, Lipton A, Brown JE, Lee KA, Smith M, Saad F, Zheng M, Hei YJ, Seaman J, Cook R. Predictive value of bone resorption and formation markers in cancer patients with bone metastases receiving the bisphosphonate zoledronic acid. *J Clin Oncol* 2005;23:4925–35.
21. Ruzicka FJ, Schmid SM, Groveman DS, Cummings KB, Borden EC. Variation in the binding of 125I-labeled interferon-beta ser to cellular receptors during growth of human renal and bladder carcinoma cells in vitro. *Cancer Res* 1987;47: 4582–9.
22. Choueiri TK, Plantade A, Elson P, Negrier S, Ravaud A, Oudard S, Zhou M, Rini BI, Bukowski RM, Escudier B. Efficacy of sunitinib and sorafenib in metastatic papillary and chromophobe renal cell carcinoma. *J Clin Oncol* 2008;26:127–31.

23. Gore ME, Szczylik C, Porta C, Bracarda S, Bjarnason GA, Oudard S, Hariharan S, Lee SH, Haanen J, Castellano D, Vrdoljak E, Schöffski P, et al. Safety and efficacy of sunitinib for metastatic renal-cell carcinoma: an expanded-access trial. *Lancet Oncol* 2009;10:757–63.
24. Schmidt L, Duh FM, Chen F, Kishida T, Glenn G, Choyke P, Scherer SW, Zhuang Z, Lubensky I, Dean M, Allikmets R, Chidambaram A, et al. Germline and somatic mutations in the tyrosine kinase domain of the MET proto-oncogene in papillary renal carcinomas. *Nat Genet* 1997;16:68–73.
25. Tomlinson IP, Alam NA, Rowan AJ, Barclay E, Jaeger EE, Kelsell D, Leigh I, Gorman P, Lamlum H, Rahman S, Roylance RR, Olpin S, et al. Germline mutations in FH predispose to dominantly inherited uterine fibroids, skin leiomyomata and papillary renal cell cancer. *Nat Genet* 2002;30:406–10.
26. Linehan WM, Pinto PA, Srinivasan R, Merino M, Choyke P, Choyke L, Coleman J, Toro J, Glenn G, Vocke C, Zbar B, Schmidt LS, et al. Identification of the genes for kidney cancer: opportunity for disease-specific targeted therapeutics. *Clin Cancer Res* 2007;13 (2 Part 2): 671–9.
27. Pennacchietti S, Michieli P, Galluzzo M, Mazzone M, Giordano S, Comoglio PM. Hypoxia promotes invasive growth by transcriptional activation of the met protooncogene. *Cancer Cell* 2003;3:347–61.
28. Isaacs JS, Jung YJ, Mole DR, Lee S, Torres-Cabala C, Chung YL, Merino M, Trepel J, Zbar B, Toro J, Ratcliffe PJ, Linehan WM, et al. HIF overexpression correlates with biallelic loss of fumarate hydratase in renal cancer: novel role of fumarate in regulation of HIF stability. *Cancer Cell* 2005;8:143–53.
29. Ljungberg BJ, Jacobsen J, Rudolfsson SH, Lindh G, Grankvist K, Rasmuson T. Different vascular endothelial growth factor (VEGF), VEGF-receptor 1 and –2 mRNA expression profiles between clear cell and papillary renal cell carcinoma. *BJU Int* 2006;98:661–7.
30. Ebos JM, Lee CR, Christensen JG, Mutsaers J, Kerbel RS. Multiple circulating proangiogenic factors induced by sunitinib malate are tumor-independent and correlate with antitumor efficacy. *Proc Natl Acad Sci USA* 2007;104:17069–74.

Embryonic Liver Morphology and Morphometry by Magnetic Resonance Microscopic Imaging

AYUMI HIROSE,[1] TAKASHI NAKASHIMA,[1] SHIGEHITO YAMADA,[2] CHIGAKO UWABE,[2] KATSUMI KOSE,[3] AND TETSUYA TAKAKUWA[1]*

[1]Human Health Science, Graduate School of Medicine, Kyoto University Kyoto, Japan
[2]Congenital Anomaly Research Center, Kyoto University Graduate School of Medicine, Kyoto, Japan
[3]Institute of Applied Physics, University of Tsukuba, Ibaragi, Japan

ABSTRACT

Embryonic liver has a unique external morphology and quantitative morphometry, based on magnetic resonance imaging data of human embryos from the Kyoto Collection of Human Embryos. Liver morphogenesis is strongly affected by the adjacent organs and tissues. The left ventricle develops to the left medial-caudal side, which results in the formation of a depression at left medial region and a prominence bilaterally at the cranial surface of the liver between Carnegie Stage (CS)17 and CS19. An imprint of the stomach that formed at the dorsal left-medial region of the liver became more marked with development until CS23. A depression induced by the umbilicus formed at the ventral region of the liver between CS16 and CS19. An indentation caused by the right adrenal gland formed at the dorsal-caudal region of the liver surface from CS20. Morphometric analysis revealed that the volume of the liver increased exponentially from CS14 through CS23. The liver developed preferentially along the dorsoventral axis and right/left axis until CS17, along the craniocaudal axis between CS17 and CS19, and then in all directions after CS19. Several important developmental phenomena, such as differentiation of the diaphragm, the extension of the body axis of the embryo, and the physiologic herniation of the intestine into the umbilical cord, may affect morphometric data. These data contribute to a better understanding of liver development as well as the morphogenesis of adjacent organs, both temporally and spatially, and serve as a useful reference for fetal medicine and prenatal diagnosis. Anat Rec, 295:51–59, 2012.

Key words: liver morphology; morphometry; human embryo; magnetic resonance imaging

Additional Supporting Information may be found in the online version of this article.

Abbreviations used: 3D = three-dimensional; CS = Carnegie stages; HV = hepatic veins; IVC = inferior vena cava; L_{CC} = craniocaudal length; L_{DV} = dorsoventral length; L_{TH} = trunk height; L_{TR} = transverse length; MR = magnetic resonance; ROI = region of interest.

Grant sponsor: Japan Society for the Promotion of Science, BIRD of Japan Science and Technology Agency (JST); Grant numbers: 22591199, 228073, 238058, 21790180.

*Correspondence to: Dr. Tetsuya Takakuwa, Human Health Science, Graduate School of Medicine, Kyoto University, 606-8507 Sakyo-ku Shogoin Kawahara-cyo 53, Kyoto, Japan. E-mail: tez@hs.med.kyoto-u.ac.jp

Received 11 March 2011; Accepted 5 September 2011
DOI 10.1002/ar.21496
Published online 18 November 2011 in Wiley Online Library (wileyonlinelibrary.com).

The liver occupies a large space in the abdominal cavity during most of the prenatal period and plays an important role in the development of functional organs (Lemaigre, 2009; Sadler and Langman, 2010). The liver becomes a hematopoietic organ after 6 weeks (Drews, 1995) and begins to metabolize important biochemical materials for development, such as albumin, bile, glycogen, and fetal-specific proteins, at around 8 weeks (Carlson, 2009).

The development of the liver proceeds in a unique manner. The liver develops at Carnegie Stage (CS) 11 (30 days after fertilization) as an outgrowth of the endodermal epithelium, the liver bud, from the caudal part of the foregut. The liver originates from two different tissues: angioblastic tissue from the coelomic surface cells and epithelial columns sprouting from the hepatic evagination of the gut epithelium (O'Rahilly and Müller, 1987). The liver lies at an active center of angiogenesis in the early embryonic period. The asymmetricity of the afferent venous vessels of the liver derives from two specific circulation systems: the vitelline and umbilical veins, which are acquired between CS13 and CS16 (Mall, 1906; Dickson, 1957; Collardeau-Frachon and Scoazec, 2008). Efferent venous vessels, including the right, left, and middle hepatic veins (HVs) and the inferior vena cava (IVC), form at similar stages. The developmental process of the efferent venous vessels is not as well studied as that of the afferent venous vessels (Mall, 1906; Dickson, 1957; Couinaud, 1996; Collardeau-Frachon and Scoazec, 2008).

Among recent three-dimensional (3D) imaging techniques, magnetic resonance (MR) microscopy is a powerful tool for 3D measurements. It is a noninvasive and nondestructive imaging method, and has been applied to analyze embryonic development in different animal models (Bone et al., 1986; Smith et al., 1992, 1994, 1996). MR imaging of embryos is highly advantageous (Effmann et al., 1988; Smith et al., 1992; Haishi et al., 2001), providing a resolution of 40 μm/pixel or better with long scan times. Kyoto and Tsukuba Universities began a project in 1999 to acquire 3D MR microscopic images of thousands of human embryos using a super-parallel MR microscope operated at 2.34T (Shiota 2007; Matsuda et al., 2003, 2007; Yamada et al., 2006).

In the present study, the precise external morphology and morphometry of the embryonic liver was studied using MR imaging data of human embryos from the Kyoto Collection of Human Embryos (http://bird.cac.med.kyoto-u.ac.jp). These data will serve as a useful reference for evaluating the development of the embryonic liver and adjacent organs and how they morphologically affect each other.

MATERIALS AND METHODS

Human Embryo Specimens

Approximately 44,000 human embryos, comprising the "Kyoto collection," are historical specimens collected and stored at the Congenital Anomaly Research Center of Kyoto University (Nishimura et al., 1968; Nishimura, 1975; Shiota, 1991; Yamada et al., 2004). In most cases, pregnancy was terminated during the first trimester of pregnancy for socioeconomic reasons under the Maternity Protection Law of Japan. Some of the specimens (~20%) are undamaged, well-preserved embryos. When the aborted materials were brought to the laboratory, the embryos were measured, examined, and staged using the criteria of O'Rahilly and Müller (1987). Approximately 1,200 well-preserved human embryos diagnosed as externally normal at CS13 to CS23 were selected for MR microscopic imaging. The conditions used to acquire the MR images of the embryos are described elsewhere (Shiota, 2007; Matsuda et al., 2003, 2007; Yamada et al., 2010).

MR Image Processing and Selection of the Datasets

3D MR image datasets for each embryo were initially obtained from 256 × 256 × 512 voxels. Each dataset was first converted into a two-dimensional (2D) stack and saved as an audio video interleave (.avi) file format using software ImageJ™ (version1.42q, National Institutes of Health, Bethesda, MD). Sequential 2D images were resectioned digitally and 3D images were reconstructed using the software OsiriX™ (version 3.7.1, Pixmeo SARL, Geneva, Switzerland). Both 2D and 3D images were carefully observed and selected according the following conditions: (1) no obvious damage or significant anomaly present in the external appearance, (2) body axes maintained in the original form that is not deformed artificially during fixation and preservation, (3) sufficiently high quality of reconstructed 2D images to properly extract the organs and tissues, and (4) liver, stomach, IVC located in the normal anatomic position.

For the present study, 67 samples were selected from the 1,200 MR image datasets based on the criteria described earlier, consisting of five cases each for CS14, CS16, CS18, CS19, CS21, and CS22; nine cases each for CS15, CS20, and CS23; and 10 cases for CS17.

3D Reconstruction of the Liver and Adjacent Organs

The avi file format images obtained from 3D MR images were resectioned digitally to the suitable planes for each analysis using the multiplanar reformatting tool in software Image J and OsiriX. Targeted organs of interest were segmented in a series of coronal-sectional images using the region of interest (ROI) module in OsiriX. 3D objects were computationally reconstructed with DeltaViewer™ (http://delta.math.sci.osaka-u.ac.jp/DeltaViewer/index-j.html; Yamada et al., 2007). Morphogenesis of the liver and adjacent organs was analyzed in detail using the 3D images (see Supporting Information Video S1, S2, S3).

Measurements of the Liver

For accurate anatomic assignment of the cranial/caudal (Z), left/right (X), and dorsal/ventral (Y) axes, the cranial/caudal axis of the liver was first determined using OsiriX. The z-axis was defined as the line that goes through the most cranial and caudal neural tubes in a series of coronal-section images that include the liver (Fig. 1A). The orthogonal plane of the z-axis was then determined and the x- and y-axes were defined as shown in Fig. 1B. Lengths of the liver along each axis

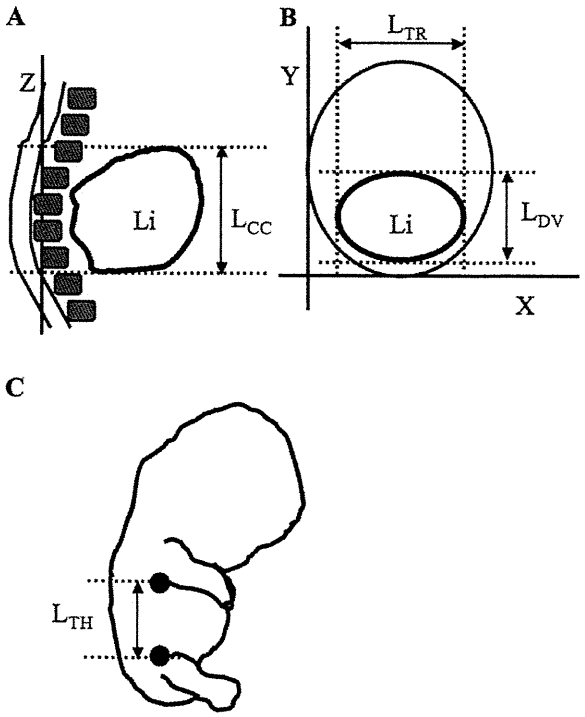

Fig. 1. Morphometry of the liver (**A,B**) An orthogonal coordinate system was defined using craniocaudal (Z)-axis, left/right (X)-axis, and dorsoventral (Y)-axis as described in the Materials and Methods section. Length of the liver along each axis was defined as craniocaudal length (L_{CC}) transverse length (L_{TR}), and dorsoventral length (L_{DV}), respectively. Li; liver (**C**) Trunk height (L_{TH}), the length between the axilla and the cranial end of the trochanterion (●),was used to measure the change in the crania-caudal growth of the abdominal cavity using the method of Otani et al. (2008) with some modification.

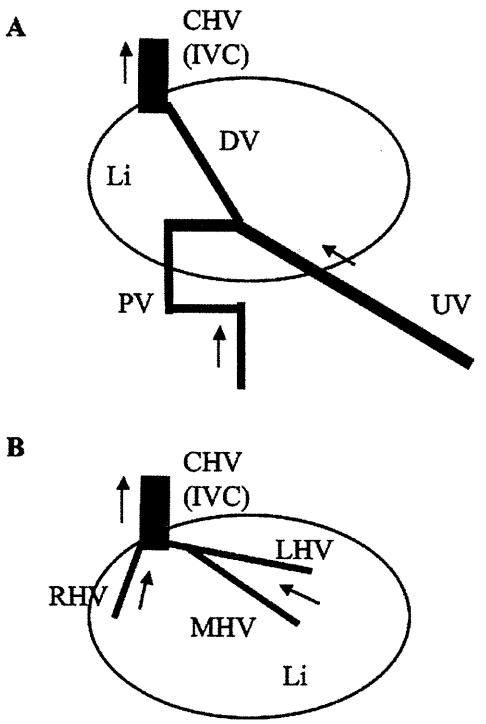

Fig. 2. Schematic representation of embryonic circulation of the liver. (**A**) Definitive afferent venous circulation of the asymmetrical stage (**B**) Definitive efferent venous vessels. Arrow indicates the direction of venous flow. Li, liver; DV, ductus venosus; PV, portal vein; UV, umbilical vein; CHV, common hepatic vein; IVC, inferior vena cava; RHV, right hepatic vein; LHV, left hepatic vein; MHV, middle hepatic vein.

were defined as the transverse length (L_{TR}), dorsoventral length (L_{DV}), and craniocaudal length (L_{CC}) (Fig. 1A,B).

The liver was extracted from a series of coronal-section images as described above. The volume of the liver was calculated by stacking the extracted liver in a series of coronal-section images using the ROI module of OsiriX. The volume of the embryo was calculated using the Region Growing module in OsiriX.

We measured trunk height (L_{TH}) as the change in the craniocaudal growth of the abdominal cavity according to a previous study by Otani et al. (2008) with some modification (Fig. 1C). In the present article, the axilla was marked instead of the acromion used by Otani et al. (2008), because the axilla was more evident on our 3D images.

Estimation of Vascular Architecture in the Liver

To elucidate the asymmetry of the afferent venous vessels, the following four vessels were reconstructed three-dimensionally; the ductus venosus, umbilical vein, portal vein, and common HV (Fig. 2A). The common HV becomes the intrahepatic part of the IVC in later stages. The three efferent venous vessels, the right, left, and middle HVs (Fig. 2B), were also estimated on 2D serially sectioned images.

RESULTS

Anatomic Relationships with the Liver

The morphogenesis of the liver was affected by the development of adjacent organs and tissues, such as the heart, diaphragm, stomach, umbilicus, abdominal wall, and adrenal gland. To elucidate the characteristic changes occurring stage- and organ-specifically, the morphogenesis of the liver is described in detail in relation to the development of adjacent organs and tissues.

Intrathoracic Organs

The right and left ventricles were at the same level along the cranial/caudal axis, and the liver was in contact with the ventricles at CS15 in the 2D image. As a consequence, the liver formed a prominence on the bilateral cranial region in all 11 cases at CS15 and CS16 (Fig. 3A-a,b). From CS17, the left ventricle developed to the left medial-caudal side, which resulted in the formation of an obvious depression in the left medial cranial region and prominences bilaterally on the cranial surface of the liver in all 11 cases (100%) between CS17 and CS19 (Fig. 3A-c,d). This depression in the left medial cranial region is a characteristic temporal feature of the

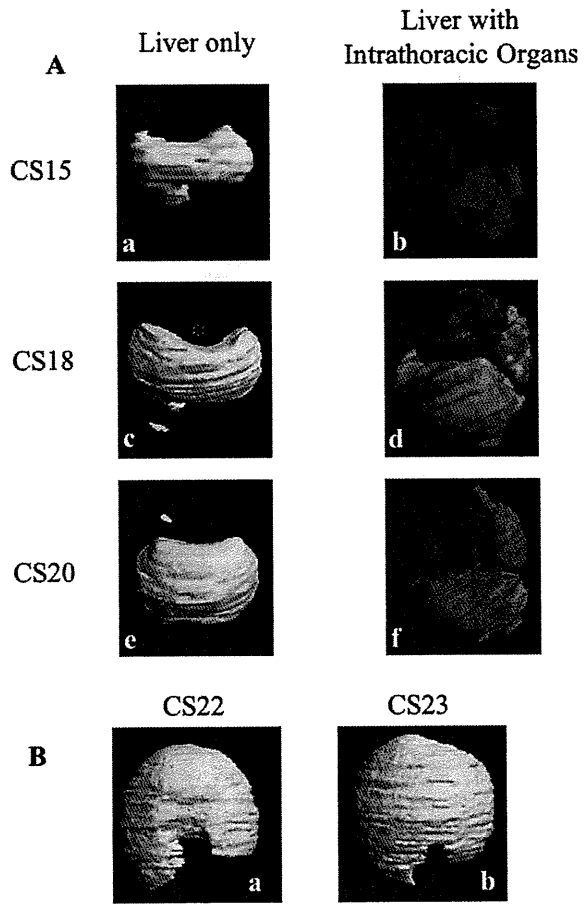

Fig. 3. Representative 3D image of the embryonic liver, demonstrating the anatomic relationship between the intrathoracic organs and the liver. (**A**) Ventral and left lateral view of the liver by 3D image between CS15 and CS20. The liver (green), lung (blue), and heart (red) were reconstructed in the picture (b, d, f). The depression formed by the left ventricle (*) is a characteristic temporal feature of the cranial surface of the liver between CS17 and CS19. (**B**) Ventral view of the liver by 3D image at CS22 and CS23. A prominence was formed in the central region of the cranial surface of the liver at CS22. The top of this prominence moved toward the right at CS23. The prominence formed by the left ventricle is a characteristic temporal feature of the cranial region of the liver at CS22 and CS23.

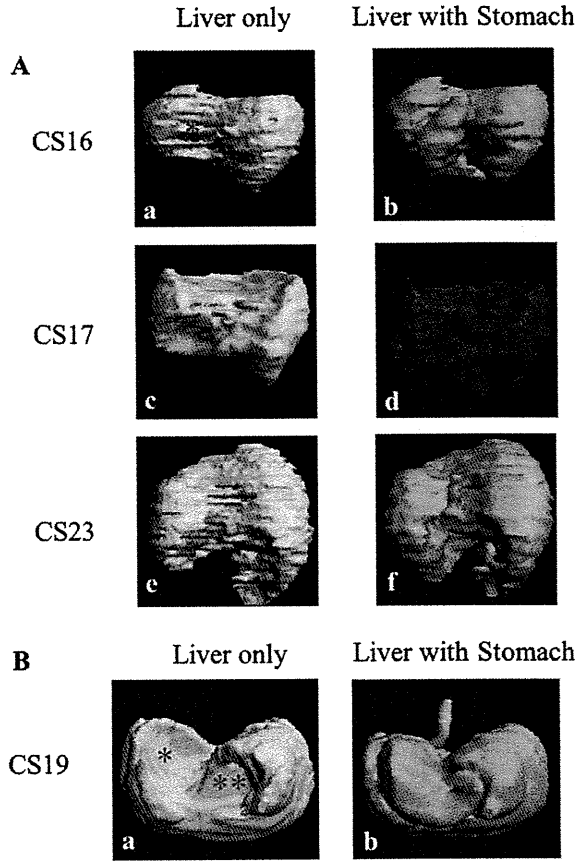

Fig. 4. Representative 3D image of the embryonic liver, demonstrating the anatomic relationship between the stomach and liver. (**A**) Dorsal view of the liver by 3D image between CS16 and CS23 The liver (green) and stomach (orange) was reconstructed (b, d, f). The "Imprint of the stomach" (*) changed according to the morphogenesis of the stomach and become deeper until CS23. (**B**) Caudal view of the liver by 3D image showing the "imprint of the stomach" (*) and "horizontal plane by pyloric-antrum" (**).

liver between CS17 and 19, and is hence termed the "heart depression." The "heart depression" was deep (maximum) until CS18, and then disappeared in 4 of 8 cases (50%) at CS20 and in 17 of 18 cases (94.4%) after CS21 (Fig. 3A-e,f). Next, the liver formed a prominence in the central region of the cranial surface in all 5 cases at CS22, as the thickness of the diaphragm was sufficiently developed to create a distinct border between the thoracic and abdominal cavities (Fig. 3B-a). The top of this prominence moved toward to the right in 7 of 8 cases (87.5%) at CS23, while the left ventricle developed left-ventrally (Fig. 3B-b).

The lung was recognized from CS14, and was in close contact with the dorsal side of the liver between CS14 and CS18 (Fig. 3A-b,d). The lung and liver were clearly separated by the developing diaphragm after CS19 in all 31 cases (Fig. 3A-f). The lung did not seem to affect the morphogenesis of the liver during development.

Stomach

The liver was deformed on the dorsal and caudal surface because of the organogenesis of the upper digestive tract, especially the stomach. The stomach formed hollows on the left-medial regions of the dorsal surface of the liver, that developed a fusiform in all 6 cases at CS15 (Fig. 4A-a,b). Then, the liver developed by covering the stomach along the greater curvature, while the stomach formed a greater and lesser curvature and rotated around in a 3D manner. As a consequence, the oral side of the stomach formed hollows on the dorsal-caudal surface of the liver in all 5 cases at CS18 (Fig. 4A-c,d). As the stomach rotated, the anal side of the stomach formed a loop, which became the pyloric

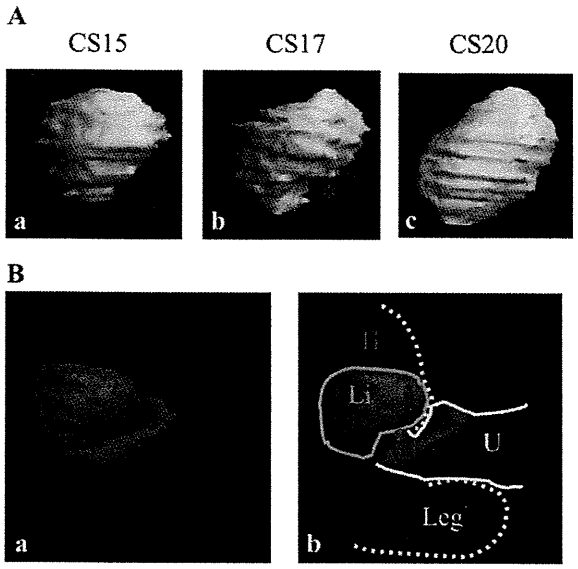

Fig. 5. Anatomic relationship between the umbilicus and liver (**A**) Representative right lateral view of the liver by 3D image between CS15 and CS20 showing the "depression by umbilicus" (*). This depression is a characteristic temporal feature at the abdominal region of the liver between CS16 and CS19. (**B**) Lateral view of the liver by 3D image at CS17 showing the relationship between the liver (Li; green) and umbilicus (U; yellow). External form of umbilicus, leg, and chest-abdominal wall is represented by the yellow and dashed lines, respectively. Red and blue circles indicate the entrances to the umbilical vein and intestinal tract, respectively.

antrum. The liver formed a "horizontal plane" by the loop on the caudal surface after CS19 in 27 of 29 cases (Fig. 4B-a,b). Marked hollows formed on the liver with development, such as the "imprint of the stomach" on the caudal surface in all 8 cases at CS23 (Fig. 4A-e,f).

Umbilicus

The part of the liver is in contact with the abdominal wall curved smoothly. The liver looked like a sector from the lateral view in 5 of 6 cases (83.3%) at CS15 (Fig. 5A-a). The liver developed along the cranial-caudal axis, and a depression formed on the ventral-medial region in all 8 cases between CS17 and CS18 (Fig. 5A-b). This depression results from the entry of the umbilical vein and intestinal tract, which herniates physiologically into the umbilical cord (Fig. 5B-a,b). The depression caused by the umbilicus disappeared in all 26 cases after CS20 because the umbilical cord moved toward the caudal side of the abdomen. Flexure of the abdomen of the embryo was evident after CS20. As a consequence, the liver looked like a quadrangle from the lateral view (Fig. 5A-c).

Retroperitoneal Organs

Retroperitoneal organs were located close to the dorsal-caudal side of the liver, but only the right adrenal gland directly contacted the liver. The adrenal gland developed remarkably up to CS19, with the right adrenal gland forming an indentation in the liver (Fig. 6A,B)

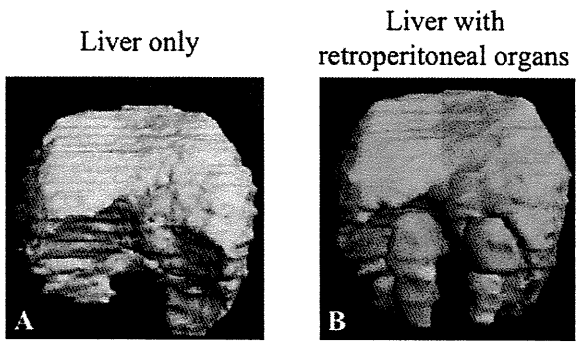

Fig. 6. Dorsal view of the 3D image of the liver at CS22 showing the anatomic relationship between the retroperitoneal organs and the liver. The liver (green), bilateral adrenal gland (purple), metanephros (yellow), and the gonads (brown) were reconstructed (B). The right adrenal gland impinged on the liver, creating an indentation (*), while the left adrenal gland remained separated from the liver by the stomach between them.

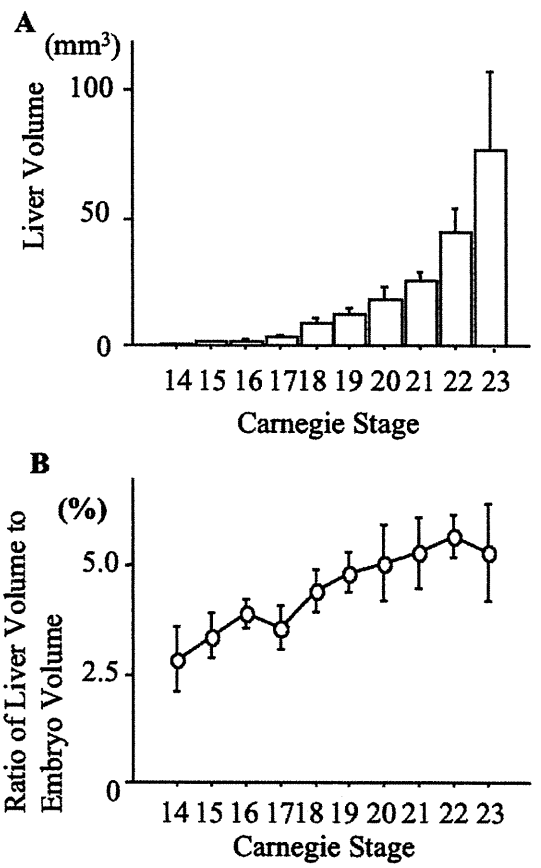

Fig. 7. Calculated liver volume of embryo from CS14 to CS23 (**A**) Liver volume was calculated as described in Materials and Methods section. Data at each CS is shown as mean ± SD mm^3 (**B**) Ratio of liver and embryo (vol/vol %). Whole embryonic volume was calculated as described in the Materials and Methods section. Data at each CS are shown as mean ± SD (%).

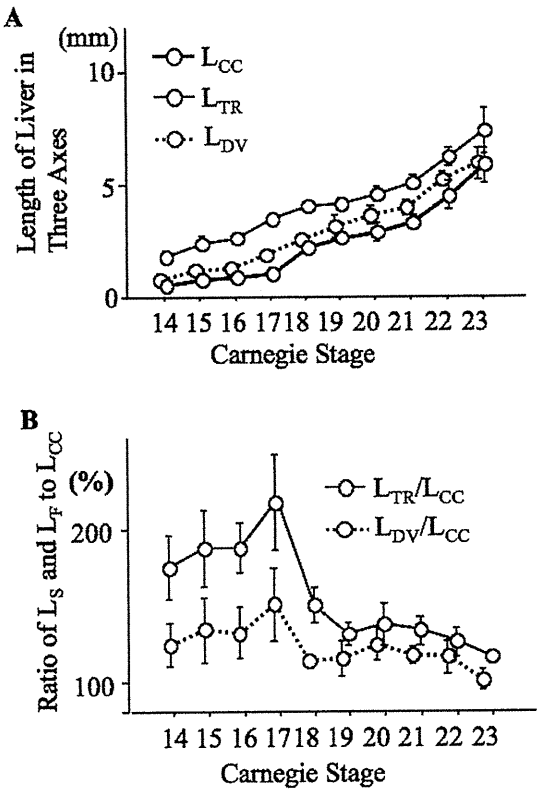

Fig. 8. Morphometry indicating the 3D direction of liver growth (**A**) Change in liver length measured along three axes between CS14 and CS23 (**B**) Ratio of transverse and dorsoventral length (L_{TR}, L_{DV}) to coronal craniocaudal length (L_{CC}) between CS14 and CS23.

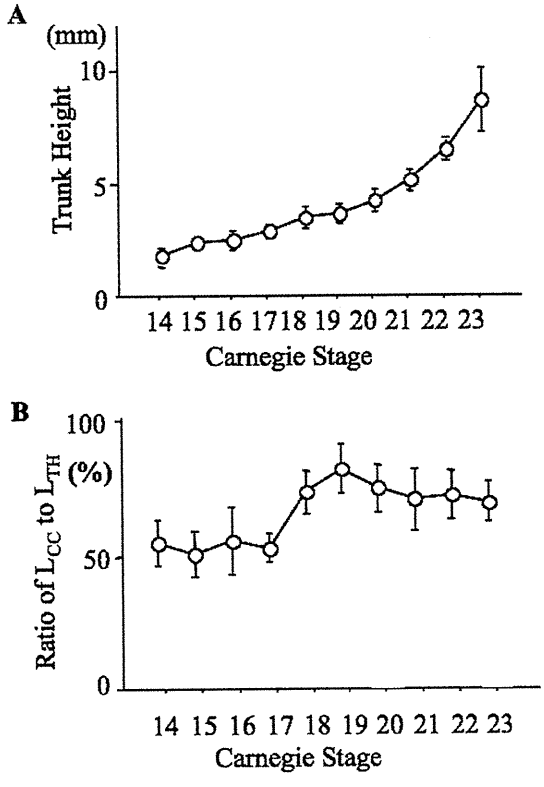

Fig. 9. Trunk height (L_{TH}) (**A**), and ratio of L_{TH} and craniocaudal length (L_{CC}) (**B**) during CS14 and CS23 embryos Trunk height (L_{TH}) was measured as a change in the cranio-caudal growth of the abdominal cavity as described in the Materials and Methods section.

in 3 of 5 cases (60%) at CS19 and in all 26 cases after CS20 in the dorsal-caudal region. The indentation formed by the adrenal gland on the liver was unilateral, only on the right side, mainly because the left adrenal gland was separated from the liver by the stomach (Fig. 6A,B). The metanephros and gonads were recognized on MR images after CS21, and seemed to contact the liver. The metanephros and gonads, however, did not seem to affect the morphogenesis of the liver in any of the 18 cases after CS21 (Fig. 6A,B).

Morphometry of the Liver

At CS14, the mean volume of the liver was 0.85 ± 0.32 mm^3 (mean ± SD) and by CS23 it had increased to 77.40 ± 31.30 mm^3 (Fig. 7A). The mean volume of the whole embryo at CS14 was 29.90 ± 7.53 mm^3, and at CS23 it had reached 1458.40 ± 433.60 mm^3. The ratio of liver volume to whole embryonic volume was 2.8 ± 0.8% at CS14, gradually increasing to 5.7 ± 0.5% at CS22 (Fig. 7B).

The length of the liver along the three axes increased exponentially, as shown in Fig. 8A. To clarify the direction of the growth of liver, the ratio of L_{TR} and L_{DV} to L_{CC} according to CS was calculated. The data revealed that the direction of the increase changed at around CS17 and CS19 (Fig. 8B). That is, the liver developed preferentially along the dorso/ventral axis and right/left axis until CS17, along the cranio/caudal axis between CS17 and CS19, and then in all directions after CS19.

L_{TH} increased from 1.84 ± 0.34 mm at CS14 to 8.68 ± 1.40 mm at CS 23 (Fig. 9A). The ratio of L_{CC} to L_{TH} was around 50% between CS14 and CS17, and then it increased to around 75% between CS18 and CS23 (Fig. 9B). The data indicated that the liver occupied about half of the abdominal cavity at CS14 and CS17, and about three-fourths of the abdominal cavity after CS18.

Vascular Architecture of the Liver

Of 62 cases from CS14 to CS23, 61 were defined as asymmetrical. The umbilical vein, portal vein, ductus venosus, and IVC were recognized in each embryo. Primary right and left HVs emerging symmetrically were identified in only one exceptional case.

The arrangement of the three terminal HVs was examined in 62 cases between CS14 and CS23 (Table 1). No HVs were identified in any of the 5 cases at CS14. All the right, left, and medial HVs were recognized between CS15 and CS23 in 39 of 57 cases (68.4%). The remaining 18 cases varied as follows: right and left HV (8 cases, 14.0%), right HV alone (1 case, 1.8%), left and

TABLE 1. Acquisition of three hepatic veins from carnegie stage 14–23

Terminal hepatic vein			Carnegie stage									
Right	Left	Middle	14	15	16	17	18	19	20	21	22	23	No. of total cases
y	y	y	0	1	2	6	4	5	7	4	4	6	39
y	y	–	0	5	2	0	1	0	0	0	0	0	8
y	–	–	0	0	0	0	0	0	0	0	0	1	1
–	y	y	0	0	1	1	0	0	1	1	1	0	5
–	y	–	0	1	0	1	0	0	0	0	0	1	3
–	–	y	0	0	0	0	0	0	0	0	0	0	0
–	–	–	5	1	0	0	0	0	0	0	0	0	6
No. of total cases			5	8	5	8	5	5	8	5	5	8	62

Acquisition of right, left, and middle hepatic veins is indicated as "y".
Five of 67 cases were unfit for estimation of vascular architecture.

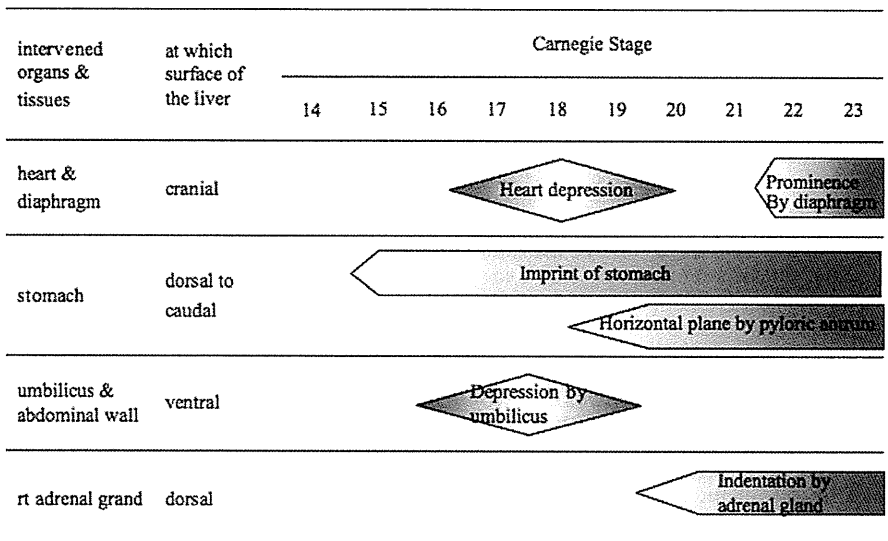

Fig. 10. Development of adjacent organs and tissues that may affect liver morphogenesis. Temporal (stage-specific) and organ-specific effects are indicated and named according to the Carnegie stage.

middle HV (5 cases, 8.7%), left HV alone (3 cases, 5.3%), and no HV (1 case, 1.8%).

DISCUSSION

The liver bud grows rapidly, and the embryonic liver occupies most of the abdominal cavity after the end of the 6th gestational week (ca. CS16; Hutchins and Moore, 1988; Lemaigre, 2009). The details of the morphologic and morphometric features of the liver during the early embryonic period, however, have remained unknown. Mall (1906) made wax models of the liver exterior from serial histologic sections of the human embryo to study the positional relationship of the gall bladder and vascular system from an outside view. He only described the morphologic changes of the liver in embryos between 17.5 and 24 mm in size; "By comparing the livers of three embryos it is seen that only their upper surfaces are regular in form from stage to stage; the processes extending into the abdominal cavity are irregular, to fit into the spaces that there are for them to grow into." Severn (1971) examined serial histologic sections of 38 human embryos from CS9 through CS11. For his detailed histologic observation, 3D drawings of the developing foregut and hepatic diverticulum were made, showing the change in the external appearance. Hutchins and Moore (1988) reported that the liver appeared at CS11 and grew to over 90 mm^3 in volume by CS23. They calculated the difference in the volume between right- and left-halves of the liver, divided by the median sagittal plane; the right half was large with an average proportion of 57.8%, and the ratio was almost constant in all embryos from CS11 through CS23. In the present study, external morphologic and morphometric analysis of the liver during embryonic periods was performed using MR imaging data acquired from embryos obtained from the Kyoto Collection. The present data revealed a unique external morphology as well as the quantitative morphometry of the embryonic liver.

Morphogenesis of the liver was strongly affected by the adjacent organs and tissues. The characteristic effects of stage- and organ-specific changes are summarized in Fig. 10. The left ventricle developed to the left medial-caudal side, which resulted in the formation of a clear depression in the left medial region and prominence bilaterally on the cranial surface of the liver between CS17 and CS19 (Fig. 3A-c,d). An imprint of the stomach formed at the

dorsal left-medial region of the liver, and became more marked with development until CS23 (Fig. 4A-a,c,e). A depression caused by the umbilicus formed in the ventral region of the liver between CS16 and CS19 (Fig. 5A-b). An indentation created by the right adrenal gland was formed at the dorsal-caudal region of the liver surface from CS20 (Fig. 6-a,b). Therefore, the morphology of the embryonic liver reflects the development of the adjacent organs during organogenesis.

Morphometric analysis in the present study revealed that the volume of the liver increased exponentially from CS14 through CS23, and the ratio of L_{TR}, L_{DV}, and L_{TH} to L_{CC} presented here indicated that the direction of growth changed at around CS17 and CS19 (Figs. 8B, 9B). That is, the liver developed preferentially along the dorso/ventral axis and right/left axis until CS17, along the cranio/caudal axis between CS17 and CS19, and then in all three directions. The occurrence of several important developmental phenomena around CS17 may affect the morphometric data (O'Rahilly and Müller, 1987; Moore, 2008; Schoenwolf and Larsen, 2009). When the septum transversum begins to differentiate into the diaphragm, development in the cranial direction is limited, while development towards the abdominal cavity is accelerated likely due to extension of the body axis of the embryo and physiologic herniation of the intestine into the umbilical cord, which creates space and transform the inner structures of the abdominal cavity (O'Rahilly and Müller, 1987).

Original and first-hand data regarding the stages of development of the vascular architecture of the liver are scarce (Collardeau-Frachon and Scoazec, 2008). Though the asymmetry of the hepatic vascular structure may be acquired between CS13 and CS16, the precise stages of development could not be determined. The right umbilical vein, which is an important indicator of the symmetrical stage, was clearly detected at CS13 (O'Rahilly and Müller, 1987). In the present study, only one case showed the right umbilical vein at CS14 and other 61 of 62 cases had already lost the right umbilical vein by CS14; that is, the hepatic vascular structure was already asymmetrical. The present data suggest that the fundamental architecture of the asymmetrical stage is acquired between CS13 and CS14 in almost embryos.

The terminal HVs formed at a similar stage as the afferent circulation system, as mentioned earlier. In the present study, three HVs were observed in 68.4% of the cases after CS15, indicating that the three HVs are acquired around CS15 in most cases. These data are consistent with those of a previous study reporting profound remodeling of the efferent venous system during the 5th gestational week (Dickson, 1957; Collardeau-Frachon and Scoazec, 2008). Three HVs were not identified until after CS17 in 19.6% of cases, suggesting that there are several individual variations in the number and arrangement of the terminal HVs, in contrast to the afferent venous circulation systems. It is so far impossible to distinguish an anomaly from a variation in individual embryos, mainly because only terminal HVs were detected on the MR image. Detailed identification of such a small branch of the vessels depends on the resolution of the imaging technique. Further improvements in imaging modalities are expected that will allow for more precise detection of the intrahepatic vascular system and application to analyses at CS13 or earlier.

Recent advances in medical imaging allow for earlier assessment of human development and prenatal diagnosis in the first trimester. Data about normal development during the embryonic stages, however, remain inadequate for guiding such clinical evaluations. Insights into the dynamic and complex processes during organogenesis will require accurate morphologic data with dynamic modeling of embryonic structures. Furthermore, 3D reconstructions are necessary to elucidate the complex anatomic remodeling that occurs during these early embryonic stages. From this point of view, the present data will be useful for evaluating the appropriate development of the embryonic liver based on the external morphology, and for evaluating adjacent organs that affect the morphology of the liver stage-specifically. This information will be an indispensable reference for clinical evaluation with obstetrical ultrasonography in the early gestational weeks, which will be useful for fetal medicine and prenatal diagnosis.

ACKNOWLEDGEMENTS

We are deeply indebted to Executive Vice President of Kyoto University, Kohei Shiota, for providing the invaluable MR data. We also acknowledge the contribution of collaborating obstetricians and the previous members of the Congenital Anomaly Research Center, Kyoto University Graduate School of Medicine.

LITERATURE CITED

Bone SN, Johnson GA, Thompson MB. 1986. Three-dimensional magnetic resonance microscopy of the developing chick embryo. Invest Radiol 21:782–787.

Carlson BM. 2009. Digestive and respiratory systems and body cavities, cardiovascular system. In: Human embryology and developmental biology. 2nd ed. Philadelphia: Mosby, Elsevier. p 353–392, 429–476.

Collardeau-Frachon S, Scoazec JY. 2008. Vascular development and differentiation during human liver organogenesis. Anat Rec 291:614–627.

Couinaud C. 1996. Translation and adaptation. 1st English ed. Surgical Anatomy of the Liver Revisited. 1st Japanese ed. Tokyo: Igaku-Shoin.

Dickson AD. 1957. The development of the ductus venosus in man and the goat. J Anat 91:358–368.

Drews U. 1995. Gastrointestinal tract. In: Color atlas of embryology. New York: Thieme Medical.

Effmann EL, Johnson GA, Smith BR, Talbott GA, Cofer G. 1988. Magnetic resonance microscopy of chick embryos in vivo. Teratology 38:59–65.

Haishi T, Uematsu T, Matsuda Y, Kose K. 2001. Development of a 1.0 T MR microscope using a Nd-Fe-B permanent magnet. Magn Reson Imaging 19:875–880.

Hutchins GM, Moore GW. 1988. Growth and asymmetry of the human liver during the embryonic period. Pediatr Pathol 8:17–24.

Lemaigre FP. 2009. Mechanisms of liver development: concepts for understanding liver disorders and design of novel therapies. Gastroenterology 137:62–79.

Mall FP. 1906. A study of structural unit of the liver. Am J Anat 5:227–308.

Matsuda Y, Utsuzawa S, Kurimoto K, Haishi T, Yamazaki Y, Kose K, Anno I, Marutani M. 2003. Super-parallel MR microscope. Magn Reson Med 50:183–189.

Matsuda Y, Utsuzawa S, Kurimoto T, Haishi T, Yamazaki Y, Kose K, Anno I, Marutani M. 2007. Imaging of a large collection of human embryo using a super-parallel MR microscope. Magn Reson Med Sci 6:139–146.

Moore KL. 2008. The digestive system. In: The developing human: clinically oriented embryology. 8th ed. Philadelphia: Saunders. p 211–242.

Nishimura H, Takano K, Tanimura T, Yasuda M. 1968. Normal and abnormal development of human embryos: first report of the analysis of 1213 intact embryos. Teratology 1:281–290.

Nishimura H. 1975. Prenatal versus postnatal malformations based on the Japanese experience on induced abortions in the human being. In: Blandau RJ, editor. Aging gametes. Basel: S Karger AG. p 349–368.

Otani H, Udagawa J, Lundh T, Hatta T, Hashimoto R, Matsumoto A, Satow F. 2008. Morphometric study on the characteristic external features of normal and abnormal human embryos. Congenit Anom (Kyoto) 48:18–28.

O'Rahilly R, Müller F. 1987. Developmental stages in human embryos: including a revision of Streeter 's "horizons" and a survey of the carnegie collection. Washington, DC: Carnegie Institution.

Sadler TW, Langman J. 2010. Cardiovascular system, digestive system. In: Langman's medical embryology. 11th ed. Philadelphia: Walters Kluwer Health, Lippincott William & Wilkins. p 165–200, 209–234.

Schoenwolf GC, Larsen WJ. 2009. Development of the gastrointestinal tract. In: Larsen's human embryology. 4th ed. Philadelphia: Churchill Livingstone: Elsevier. p 435–477.

Severn CB. 1971. A morphological study of the development of the human liver. I. Development of the hepatic diverticulum. Am J Anat 131:133–158.

Shiota K. 1991. Development and intrauterine fate of normal and abnormal human conceptuses. Congenit Anom (Kyoto) 31:67–80.

Shiota K, Yamada S, Nakatsu-Komatsu T, Uwabe C, Kose K, Matsuda Y, Haishi T, Mizuta S, Matsuda T. 2007. Visualization of human prenatal development by magnetic resonance imaging (MRI). Am J Med Genet A 143A:3121–3126.

Smith BR, Effmann EL, Johnson GA. 1992. MR microscopy of chick embryo vasculature. J Magn Reson Imaging 2:237–240.

Smith BR, Johnson GA, Groman EV, Linney E. 1994. Magnetic resonance microscopy of mouse embryos. Proc Natl Acad Sci U S A 91:3530–3533.

Smith BR, Linney E, Huff DS, Johnson GA. 1996. Magnetic resonance microscopy of embryos. Comput Med Imaging Graph 20:483–490.

Yamada S, Uwabe C, Fujii S, Shiota K. 2004. Phenotypic variability in human embryonic holoprosencephaly in the Kyoto Collection. Birth defects research. A Clin Mol Teratol 70:495–508.

Yamada S, Uwabe C, Nakatsu-Komatsu T, Minekura Y, Iwakura M, Motoki T, Nishimiya K, Iiyama M, Kakusho K, Minoh M, Mizuta S, Matsuda T, Matsuda Y, Haishi T, Kose K, Fujii S, Shiota K. 2006. Graphic and movie illustrations of human prenatal development and their application to embryological education based on the human embryo specimens in the Kyoto collection. Dev Dyn 235:468–477.

Yamada S, Itoh H, Uwabe C, Fujihara S, Nishibori C, Wada M, Fujii S, Shiota K, 2007. Computerized three-dimensional analysis of the heart and great vessels in normal and holoprosencephalic human embryos. Anat Rec (Hoboken). 290:259–267.

Yamada S, Samtani RR, Lee ES, Lockett E, Uwabe C, Shiota K, Anderson SA, Lo CW. 2010. Developmental atlas of the early first trimester human embryo. Dev Dyn 239:1585–1595.

Archives of Gerontology and Geriatrics 54 (2012) e102–e108

Contents lists available at SciVerse ScienceDirect

Archives of Gerontology and Geriatrics

journal homepage: www.elsevier.com/locate/archger

Maladaptive turning and gaze behavior induces impaired stepping on multiple footfall targets during gait in older individuals who are at high risk of falling

Minoru Yamada [a,*], Takahiro Higuchi [b], Shuhei Mori [a], Kazuki Uemura [c], Koutatsu Nagai [a], Tomoki Aoyama [a], Noriaki Ichihashi [a]

[a] Department of Human Health Sciences, Kyoto University Graduate School of Medicine, 53 Kawahara-cho, Shogoin, Sakyo-ku, Kyoto 606-8507, Japan
[b] Department of Health Promotion Science, Graduate School of Human Health Science, Tokyo Metropolitan University, 1-1 Minami-Ohsawa, Hachioji, Tokyo 192-0397, Japan
[c] Department of Physical Therapy, Graduate School of Medicine, Nagoya University, 1-1-20 Daikouminami, Higashi-ku, Nagoya 461-8673, Japan

ARTICLE INFO

Article history:
Received 18 June 2011
Received in revised form 18 August 2011
Accepted 20 August 2011
Available online 9 September 2011

Keywords:
Gaze behavior
Falls
Older
MTST

ABSTRACT

It was recently reported that the measurement of stepping accuracy while performing a new walking test, a multi-target stepping task (MTST), could contribute to identifying older individuals at high risk (HR) of falling. The present study was designed to identify factors leading HR older individuals to an impaired stepping performance in terms of frequency of maladaptive turning behavior (spin turn) and spatio-temporal patterns of fixations. Eleven HR (80.8 ± 3.6 years), 26 low-risk (LR) (77.1 ± 7.7 years) older individuals, and 20 younger individuals performed the MTST. For the MTST, stepping accuracy was measured with two types of failure (stepping target and avoiding distracters). The frequency of a spin turn (i.e., a crossover step) was compared among the groups. The location and duration of each fixation were also compared. The HR older and younger participants showed a higher rate of spin turns. Whereas the younger participants fixated approximately three steps ahead, the older participants directed their fixation closer toward the imminent footfall target, demonstrating their difficulty to use the visual information regarding the target in a feedforward manner. Such patterns of fixations were significantly associated with the frequency of stepping and avoidance failures. The higher rate of stepping and avoidance failures in the MTST were attributed to maladaptive turning behavior, which is potentially destabilizing, and the tendency to fixate on/around an imminent footfall target, which prevented older individuals from considering the locations of future footfall targets.

1. Introduction

Older individuals who are at high risk for a fall generally exhibit increased gait variability (Verghese et al., 2009; Brach et al., 2010), a decline in visuomotor control of foot movement (Chapman and Hollands, 2006a,b, 2007), and cognitive impairment, particularly in executive functions (Alexander et al., 2005; Persad et al., 2008; Herman et al., 2010). As a result, when instructed to step precisely on a footfall target on the ground, they show more impaired performance than older individuals who are at low risk for a fall (Chapman and Hollands, 2006b, 2007). Measurement of stepping accuracy during gait is therefore useful as a clinical tool to distinguish HR older individuals from LR older individuals.

Recently, we developed a new clinical test, a multi-target stepping task, to measure the stepping accuracy in a simplified manner (Yamada et al., 2011). In the MTST, participants were instructed to step on an assigned square (the footfall target) continuously along the 15 lines while avoiding the other squares (distracters). The results demonstrated that 64.5% of HR older participants failed to step precisely on the target at least once (referred to as a stepping failure). The HR older participants also showed a significantly higher rate of failure to avoid stepping on distracters (avoidance failure) than LR older participants. A logistic regression analysis showed a significantly high odds ratio for the stepping failure (19.365), although the very large range of 95% CI (3.28–113.95) indicated that the results need to be interpreted cautiously. These findings led us to the tentative conclusion that measuring the stepping accuracy while performing the MTST is potentially an important factor in the identification of HR older individuals.

Understanding factors contributing to enhance a predictive power of the MTST to identify HR older individuals is necessary for its clinical use and a development of an intervention technique to improve stepping accuracy while performing the MTST. For this purpose, the present study was designed to measure two behaviors while performing the MTST: turning and gaze behavior.

Inaccurate stepping performance may well result from maladaptive strategies for stepping in a different direction, i.e.,

* Corresponding author. Tel.: +81 75 751 3964; fax: +81 75 751 3909.
E-mail address: yamada@hs.med.kyoto-u.ac.jp (M. Yamada).

0167-4943/$ – see front matter © 2011 Elsevier Ireland Ltd. All rights reserved.
doi:10.1016/j.archger.2011.08.012

turning behavior. The placement of multiple targets in the MTST could lead participants to turn quickly in a different direction. HR older individuals generally show difficulty in maintaining a stabilized posture after stepping in a different direction (Dite and Temple, 2002; Tseng et al., 2009). Two main strategies for turning exist: step and spin turns. Whereas a step turn involves a change in the direction opposite to the stance limb, the spin turn is taking a crossover step, i.e., changing in the direction toward the same side of the stance limb. A spin turn is potentially destabilizing because, if appropriate pro-active action is not taken, the center of mass (COM) of the body will be outside of the base of support (BOS) (Moraes et al., 2004; Taylor et al., 2005). We hypothesized that impaired stepping performance while performing the MTST in HR older individuals was accompanied by more frequent spin turns.

Spin turns could occur more frequently when participants concentrated on stepping accurately on an imminent footfall target and did not consider the locations of future footfall targets. Measuring gaze behavior while performing the MTST was an effective approach to address this issue. By measuring how far ahead the fixation was located, we examined whether age-related differences existed in the visual scanning of footfall targets while performing the MTST.

The hypothesis regarding the location of fixation was that fixation in older individuals should be directed closer toward an imminent footfall target. The spatial demand of stepping in the MTST is relatively moderate, considering the criteria that even a step on the edge of the target was regarded as successful. Under such moderate conditions, younger individuals generally fixate a few steps ahead to step on multiple footfall targets (Patla and Vickers, 2003). This means that visual information regarding the location of an imminent footfall target is used in a feedforward manner, i.e., based on "stored" visuospatial information (Zettel et al., 2008), rather than in an on-line, feedback manner. In contrast, older individuals have difficulty using vision in a feedforward manner (Chapman and Hollands, 2006a). It was therefore hypothesized that fixation in older individuals should be directed closer toward an imminent footfall target.

To further understand the characteristics of gaze behavior in HR older individuals, we examined the duration of each fixation, particularly toward a target. Chapman and colleagues demonstrated that HR older individuals looked at targets longer when they walked while stepping on multiple footfall targets with relatively strict spatial demand (Chapman and Hollands, 2006b, 2007). With these findings, they proposed that they would require more time to process visual information regarding targets and/or program appropriate motor responses. We investigated whether a similar tendency would occur while they performed the MTST in spite of its moderate spatial demand.

Our primary analyses were to compare stepping performances, turning and gaze behaviors among the HR older, LR older, and the younger control groups. In addition, it was important to address which of several measurements were significantly associated with stepping avoidance failures. To do so, secondary analyses were conducted. Older participants were divided into two groups according to whether they had experienced stepping and avoidance failures (i.e., regardless of whether they were in the HR or older LR group). Each measurement regarding gaze behavior and other clinical measurements were compared statistically between the two groups. Furthermore, to determine whether the maladaptive spin turn occurred as a result of the participants' fixation being directed closer to the target, we conducted another statistical analysis in which the older participants were divided into two groups according to their experience of the spin turn. Comparisons of the gaze behavior were made between the two groups.

2. Methods

2.1. Participants

A total of 37 community-dwelling older individuals (mean age, 78.1 ± 6.8 years) participated. The exclusion criteria ensured that none of the participants had any indications of the following symptoms: (a) serious visual impairment (cataract, glaucoma, or color blindness), (b) inability to ambulate independently (those requiring the assistance of a walker were excluded), (c) score of less than 7 on the Rapid Dementia Screening Test (Kalbe et al., 2003), (d) symptomatic cardiovascular disease, (e) neurological and orthopedic disorders, (f) peripheral neuropathy of the lower extremities, or (g) severe arthritis. None of them had performed the MTST before. Twenty younger individuals (mean age, 21.1 ± 1.4 years) also took part in this experiment as control participants. Written informed consent was obtained from each subject in accordance with the guidelines approved by the Kyoto University Graduate School of Medicine and the Declaration of Human Rights, Helsinki, 1975.

Following an earlier study (Yamada et al., 2011), a participant who met the following two criteria was classified as an HR older individual: (a) a self-report of the occurrence of at least one fall within the past year and (b) a time requirement greater than 13.5 s for performing a Timed Up and Go test (TUG) (Shumway-Cook et al., 2000). A fall was defined as any event that led to an unplanned, unexpected contact with a supporting surface during walking. Our definition that the experience of falls was restricted to those during walking (i.e., falls during standing or transferring were not included) was suitable for the present study, considering that the MTST was developed to differentiate older HR individuals from LR ones in terms of stepping accuracy during walking. We ensured that none of the participants had any fall experience during standing or transferring.

As a result, 11 HR and 26 LR elderly individuals participated (see Table 1 for participant details). A one-way ANOVA conducted for each data of age, height, weight, the score of the Rapid Dementia Screening Test, and the visual acuity score (binocular acuity scored on the basis of a Landolt C) showed no significant differences between the HR and LR groups (Table 1). A Chi-square analysis conducted for the data of gender distribution also showed no significant differences between the HR and LR groups (Table 1).

2.2. Setup and protocols for data collection of the MTST

The MTST was performed on a black elastic mat (10 m long and 1 m wide). There were 45 pieces of a 10 cm × 10 cm square on the mat (see Fig. 1a). These squares were arranged into three rows (15 cm between each row) and 15 lines (61 cm between each line). Each square was marked with red, blue, or yellow tape. Each line had one of the three colored squares in a randomized order. One square (blue or yellow) was regarded as a footfall target, while the others were distracters.

Gaze behavior was measured using a head-mounted eye tracker (EMR-9, Nac Image Technologies, Japan). The eye tracker we used was a binocular corneal reflection system that measures the eye line of gaze with respect to a hat. The participant's gaze was indicated by a circle mark on a video-based image of the visual field as recorded by a scene camera mounted on the hat at a temporal resolution of 30 Hz (see Fig. 1b). Three-dimensional accelerometers (WAA-006, ATR-Promotions, Japan) were attached to each heel to measure the timing of participants' heel contact for each stepping.

The participants wore flat-soled footwear and walked on the mat at a self-selected pace while stepping on the target square placed on each line without stepping on the distracters. The participants performed two main trials. For each trial, a different color square was assigned as a footfall target. Detailed information